

# Carderock Division, Naval Surface Warfare Center

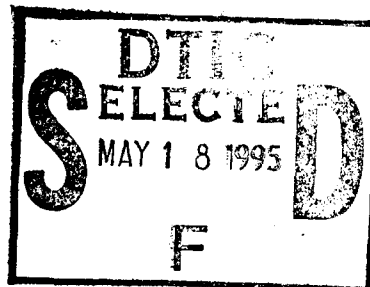
Bethesda, MD 20084-5000

CDRKNWC/HD-1427-01 October 1994

Hydromechanics Directorate  
Directorate Report

## A Simulation of Viscous Incompressible Flow Through a Multiple-Blade-Row Turbomachinery with a High-Resolution Upwind Finite-Differencing Scheme

by  
Cheng-I Yang



19950517 075



DTIC QUALITY INSPECTED 5

Approved for public release; distribution is unlimited.

CDRKNWC/HD-1427-01 A Simulation of Viscous Incompressible Flow Through a Multiple-Blade-Row Turbomachinery with a High-Resolution Upwind Finite-Differencing Scheme

## MAJOR CARDEROCK DIVISION TECHNICAL COMPONENTS

- CODE 011 Director of Technology
- 10 Machinery Systems/Programs and Logistics Directorate
  - 20 Ship Systems and Programs Directorate
  - 50 Hydromechanics Directorate
  - 60 Survivability, Structures and Materials Directorate
  - 70 Signatures Directorate
  - 80 Machinery Research and Development Directorate
  - 90 Machinery In-Service Engineering Directorate

### CARDEROCK DIVISION, NSW, ISSUES THREE TYPES OF REPORTS:

1. **CARDEROCKDIV reports, a formal series**, contain information of permanent technical value. They carry a consecutive numerical identification regardless of their classification or the originating directorate.
2. **Directorate reports, a semiformal series**, contain information of a preliminary, temporary, or proprietary nature or of limited interest or significance. They carry an alphanumerical identification issued by the originating directorate.
3. **Technical memoranda, an informal series**, contain technical documentation of limited use and interest. They are primarily working papers intended for internal use. They carry an identifying number which indicates their type and the numerical code of the originating directorate. Any distribution outside CARDEROCKDIV must be approved by the head of the originating directorate on a case-by-case basis.



DEPARTMENT OF THE NAVY  
NAVAL SURFACE WARFARE CENTER  
CARDEROCK DIVISION

CARDEROCK DIVISION HEADQUARTERS  
DAVID TAYLOR MODEL BASIN  
9500 MACARTHUR BOULEVARD  
WEST BETHESDA, MD 20817-5700

*Errata*

IN REPLY REFER TO:  
5605  
506 Ser 89  
09 OCT 1989

From: Commander, Carderock Division, Naval Surface Warfare Center  
To: Distribution

Subj: CHANGE IN REPORT NUMBER

1. The Report entitled, "A Simulation of Viscous Incompressible Flow Through a Multiple-Blade-Row Turbomachinery with a High-Resolution Upwind Finite-Differencing Scheme," by Cheng-I Yang was published with report number CDRKNSWC/HD-1427-01. The report number was given in error and should be changed to **CDRKNSWC/HD-1453-01**.

2. Please make the change on your copy of the report.

*Wm. B. Morgan*  
Wm. B. MORGAN  
By direction

Distribution:

ARPA  
ONR 333 (Purtell, Rood)  
ONR 334 (Tucker)  
OPNAV N87S  
NAVSEA  
03H  
03X  
03T (M. Nicholson)  
PEO-SUB R (Spero, Troffer, Robinson)  
PEO-SUB X (Becker)  
NUWS (P. LeFebvre, J. Uhlman)  
DTIC  
SAIC (Korpus)  
MIT/Dept Ocean Eng. (Keenan, Kerwin)  
NNS (J. DeNuto)  
GD/EB (M. King)  
PSU/ARL (Knight, McBride, Zierke)

19950517075

A 294309

UNCLASSIFIED

SECURITY CLASSIFICATION OF THIS PAGE

## REPORT DOCUMENTATION PAGE

1a. REPORT SECURITY CLASSIFICATION <b>UNCLASSIFIED</b>		1b. RESTRICTIVE MARKINGS	
2a. SECURITY CLASSIFICATION AUTHORITY		3 DISTRIBUTION/AVAILABILITY OF REPORT Approved for public release; distribution is unlimited.	
2b. DECLASSIFICATION/DOWNGRADING SCHEDULE			
*4. PERFORMING ORGANIZATION REPORT NUMBER(S)  CDRK/NSWC/HD-1427-01		5. MONITORING ORGANIZATION REPORT NUMBER(S)	
6a. NAME OF PERFORMING ORGANIZATION Carderock Division Naval Surface Warfare Center	6b. OFFICE SYMBOL (If applicable)  Code 544	7a. NAME OF MONITORING ORGANIZATION	
6c. ADDRESS (City, State, and ZIP Code)  Bethesda, MD 20084-5000		7b. ADDRESS (CITY, STATE, AND ZIP CODE)	
8a. NAME OF FUNDING/SPONSORING ORGANIZATION Naval Sea Systems Command	6b. OFFICE SYMBOL (If applicable) PEO SUB-X	9. PROCUREMENT INSTRUMENT IDENTIFICATION NUMBER	
8c. ADDRESS (City, State, and ZIP code)  2531 Jefferson Davis Highway, NC-3 Arlington, VA 22242-5160		10. SOURCE OF FUNDING NUMBERS	
		PROGRAM ELEMENT NO.  63561N	TASK NO.  
		TASK NO.  	WORK UNIT ACCESSION NO.  
11. TITLE (Include Security Classification) A Simulation of Viscous Incompressible Flow Through a Multiple-Blade-Row Turbomachinery with a High-Resolution Upwind Finite-Differencing Scheme			
12. PERSONAL AUTHOR(S) Yang, Cheng-I			
13a. TYPE OF REPORT Final	13b. TIME COVERED FROM TO	14. DATE OF REPORT (Year, Month, Day) October 1994	15. PAGE COUNT
16. SUPPLEMENTARY NOTATION			
17. COSATI CODES		18. SUBJECT TERMS (Continue on Reverse if Necessary and Identify by Block Number)	
FIELD	GROUP	SUB-GROUP	
19. ABSTRACT (Continue on reverse if necessary and identify by block number)			
<p>This report investigates the feasibility of a numerical solution for a incompressible viscous flow through a multiple-blade-row turbomachinery. The numerical method used is a three-dimensional incompressible Navier-Stokes solver based on flux-difference splitting, and an implicit high-resolution scheme. In order to validate the numerical predictions, the measurements from a preswirl High Reynolds Number Pump (HIREP) experiment are selected for the purpose of comparisons. Comparisons between predictions and measurements are presented. The comparisons include the surface pressure distribution, the wake behind the trailing edge, and flow visualization on the hub and blade surfaces.</p>			
20. DISTRIBUTION/AVAILABILITY OF ABSTRACT <input type="checkbox"/> UNCLASSIFIED/UNLIMITED <input checked="" type="checkbox"/> SAME AS RPT. <input type="checkbox"/> DTIC USERS		21. ABSTRACT SECURITY CLASSIFICATION <b>UNCLASSIFIED</b>	
22a. NAME OF RESPONSIBLE INDIVIDUAL Cheng-I Yang		22b. TELEPHONE (Include Area Code) (301) 227-4307	22c. OFFICE SYMBOL Code 544

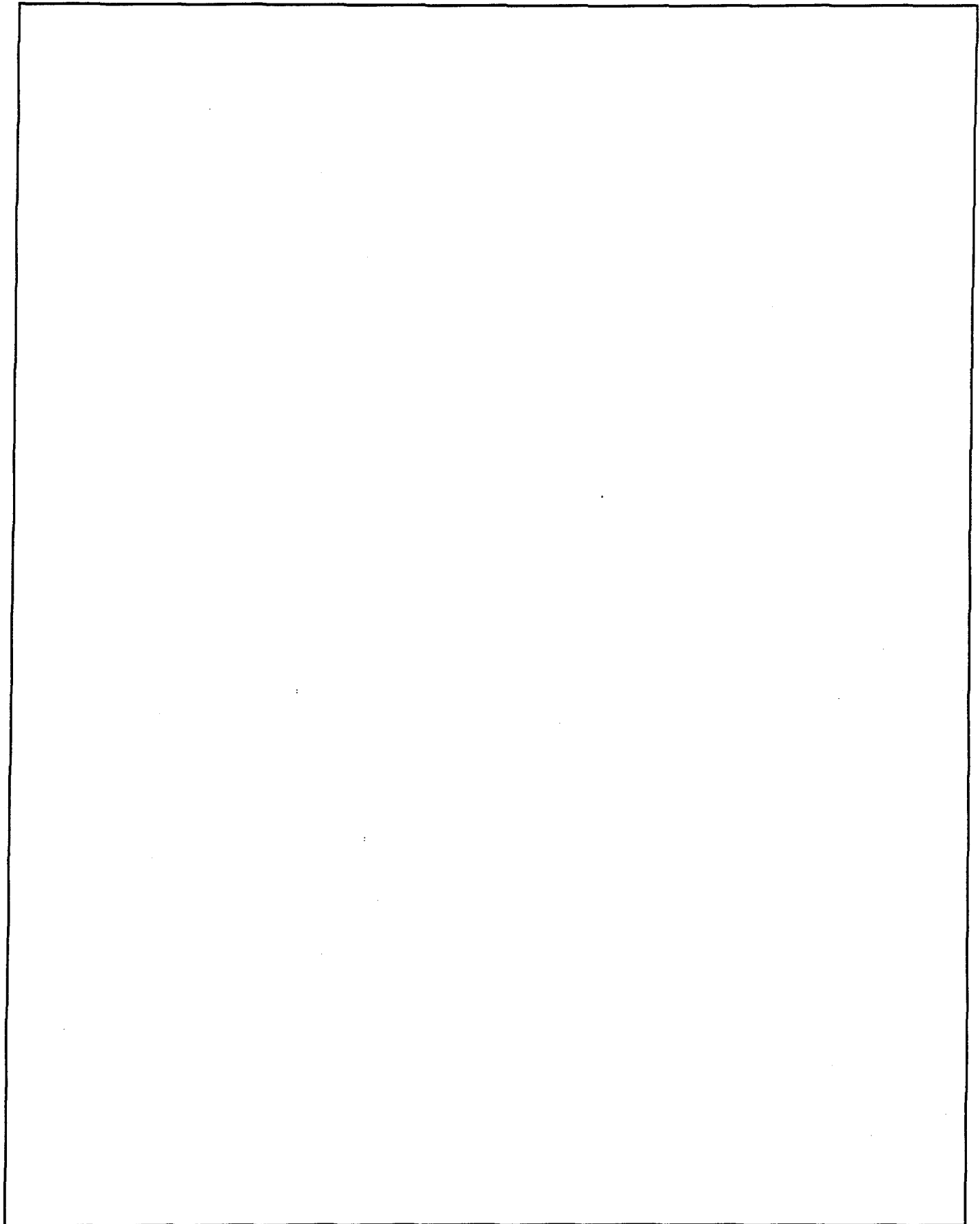
DD FORM 1473, 84 MAR

UNCLASSIFIED

SECURITY CLASSIFICATION OF THIS PAGE

UNCLASSIFIED

SECURITY CLASSIFICATION OF THIS PAGE



UNCLASSIFIED

SECURITY CLASSIFICATION OF THIS PAGE

## CONTENTS

Abstract .....	Page 1
Administrative Information .....	1
Introduction .....	1
Description of Experiment .....	2
Numerical Approximation .....	3
Motion Relative to a Rotating Reference Frame .....	4
Temporal Differencing .....	6
Spatial Differencing .....	6
Turbulence Model .....	7
Grid Topologies and Boundary Conditions .....	8
Solution Procedure .....	8
Results .....	10
IGV Passage .....	10
Rotor Passage .....	13
Conclusions and Recommendations .....	19
References .....	20

## FIGURES

1. Surface definition of IGV and rotor blade .....	3
2. Surface grids in blade passages .....	9
3. Secondary velocity vectors 49.7 percent chord axially downstream of the IGV trailing edge .....	11
4. Passage-averaged IGV wakes 49.7 percent chord axially downstream of the IGV trailing edge .....	12
5. Circumferentially averaged velocities 49.7 percent chord axially downstream of the IGV trailing edge .....	12
6. Static pressure distribution on the IGV blade surface .....	14
7. Surface flow visualization on the IGV hub surface .....	14

# FIGURES (Cont'd)

	Page
8. Surface flow visualization on the IGV blade surface .....	15
9. Circumferential variation of velocity components 32.2 percent chord axially downstream of the rotor tip trailing edge .....	16
10. Static pressure distribution on the rotor surface .....	17
11. Predicted secondary velocity at 37.8 percent chord axially downstream of the rotor tip trailing edge .....	17
12. Surface flow visualization on the rotor hub surface .....	18
13. Surface flow visualization on the suction side surface of the rotor blade .....	18
14. Particle traces of the flow through rotor tip gap .....	19

Accession For	
NTIS CRA&I	<input checked="" type="checkbox"/>
DTIC TAB	<input type="checkbox"/>
Unannounced	<input type="checkbox"/>
Justification .....	
By .....	
Distribution / .....	
Availability Codes	
Dist	Avail and/or Special
A-1	

## ABSTRACT

*This report investigates the feasibility of a numerical solution for a incompressible viscous flow through a multiple-blade-row turbomachinery. The numerical method used is a three-dimensional incompressible Navier-Stokes solver based on flux-difference splitting, and an implicit high-resolution scheme. In order to validate the numerical predictions, the measurements from a pre-swirl High Reynolds Number Pump (HIREP) experiment are selected for the purpose of comparisons. Comparisons between predictions and measurements are presented. The comparisons include the surface pressure distribution, the wake behind the trailing edge, and flow visualization on the hub and blade surfaces.*

## ADMINISTRATIVE INFORMATION

This investigation was authorized by the Naval Sea Systems Command under the NSSN Propulsor Development Program, in accordance with Program Element 63561N, Task Area 52177002, and Work Request Number N0002494WR1032788. This work was performed under DTMB Work Unit 5080-053.

## INTRODUCTION

Due to the recent advancements on the subject of the Computational Fluid Mechanics (CFD) and the availability of high speed computing machines, various Navier-Stokes solvers are used to simulate relatively complicated flow phenomenon with encouraging successes. A proper application of an accurate and reliable numerical procedure can often guide the designer of a flow machinery to identify and to avoid potential difficulties, and help to select the most favorable and innovative configurations for model testings. The attractive benefits of a successful simulation are reducing the cost and the cycling time of the design. The purpose of this report is to explore the feasibility of a numerical solution for the flow through a complicated and practical multiple-blade-row pump configuration and to evaluate the accuracy of the solutions by comparing them with the available data.

In order to validate the numerical predictions, the measurements from a pre-swirl High Reynolds Number Pump (HIREP) experiment are selected for the purpose of comparisons. The HIREP experiment was conducted at the the Garfield Thomas water tunnel at Pennsylvania State University under the sponsorship of the Advanced Research Project Agency (ARPA). One of the purposes of the experiment is to provide a data base for numerical simulations. The techniques and the uncertainties of the measurement were well documented,<sup>1</sup> hence, the reported data are suitable for validating the method of computational fluid dynamics (CFD). Because both the separation and a significant amount of the secondary flow are driven by viscous effects in the boundary

layer at the end wall regions, a Reynolds Averaged Navier-Stokes (RANS) type solver is needed. At present, a three-dimensional Navier-Stokes solver for incompressible flow based on an implicit high-resolution finite-differencing scheme suggested by Harten,<sup>2</sup> Yee et al.,<sup>3</sup> and Hartwich et al.<sup>4</sup> is employed for this purpose. The solution is limited to the steady-state case. The comparisons between predictions and measurements include the surface pressure distribution, the wake behind the trailing edge, and flow visualization on the hub and blade surfaces.

Recently, similar viscous simulations were performed by Dreyer and Zierke,<sup>5</sup> and by Lee et al.<sup>6</sup> To obtain a numerical solution, the former used a cell-center finite-volume technique with an explicit multistage time integration procedure,<sup>7</sup> and the latter used a pressure-based implicit relaxation method.<sup>8</sup>

## DESCRIPTION OF EXPERIMENT

The experiment described next is one of many that were conducted at the HIREP facility. The data obtained from this experiment are compared with the results of the numerical simulation. Only the relevant informations about the geometry of the configuration and uncertainties of the measurements are given in detail.

HIREP is a pre-swirl unit with 13 IGV blades and 7 after skew rotor blades. The radii of the hub and casing are constant at 26.67 cm. (10.5 in.) and 53.34 cm. (21 in.), respectively. This gives an annular area through the pump of 0.67 m<sup>2</sup> (7.22 ft<sup>2</sup>). The inlet guide vanes have a constant chord length of 17.53 cm. (6.90 in.) and a solidity ranging from 1.36 at the hub to 0.68 at the tip. The rotor blades have a chord length of 28.50 cm. (11.22 in.) and solidity of 1.19 at the hub, and a chord length of 26.64 cm. (10.49 in.) and a solidity of 0.56 at the tip. All the blades have fillets at the junctures. The gap clearance between the blade tip and the casing is 0.130 in. The distance between the IGV and rotor stack-up lines is 40.28 cm. (15.86 in.) Figure 1 shows a set of IGV and rotor blades (looking from upstream to downstream). The surface definition of the stator blade is given in 53 sections, each section contains 41 nodes. The surface definition of the rotor blade is given in 53 sections, each section contains 36 nodes. Grid lines shown in Fig. 1 were used to create a smooth surface with a B-spine method. Based on this smooth surface, a system of new surface grid lines suitable for viscous computation was then generated.

While this particular experiment was conducted, the rotor turned at its design point of 260 revolutions per minute (rpm), the corresponding speed at the blade tip is 14.51 m/s (47.6 ft/s). The reference velocity used as a monitor velocity during the entire experiment is 10.63 m/s (35.0 ft/s). The Reynolds number based on the reference velocity and the IGV chord length is 2.3 million. The time averaged static pressures on both the IGV and the rotor blade surfaces were measured by pressure taps which were distributed in five spanwise rows corresponding to nominal locations of 10, 30, 50, 70, and 90 percent of the span. The overall uncertainty in measurements ranged from 413.64 pascal (0.06 psi) over regions of minimal streamwise pressure gradients to

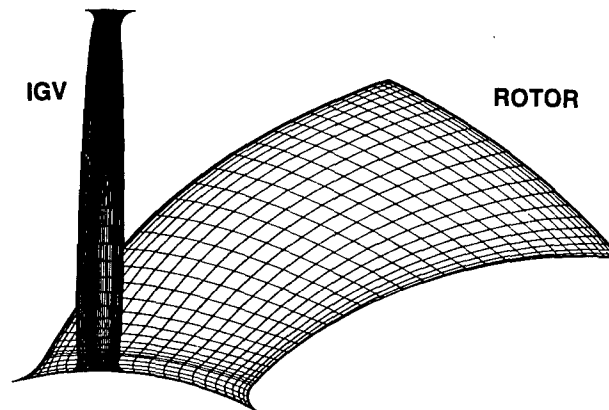


**Fig. 1.** Surface definition of IGV and rotor blades.

896.22 pascal (0.13 psi) over regions of large streamwise gradients. A radial survey of the time averaged static pressure, stagnation pressure and velocity components with a five-hole probe were conducted at 37 percent of the chord length upstream of the IGV leading edge (defined as the IGV inlet plane) and at 49.7 percent chord downstream of the IGV trailing edge (defined as the IGV exit plane). At a given circumferential location, measurements were taken at 50 different radii. In order to obtain better resolution in the circumferential direction, a five-hole probe rake was devised. This rake was used to take measurements at the IGV exit plane at 12 radial locations. At each radial location, the 360 deg survey was divided into 966 increments of 0.373 deg. The percentage uncertainty for the five-hole rake is 2.6, 9.8, and 9.9 percent for the axial velocity, the radial velocity, and the tangential velocity, respectively.

The Laser Doppler Velocimetry method (LDV) was used to measure the axial and tangential velocity components both upstream and downstream of the rotor blade row. The measurement planes were located at 26.7 percent chord axially upstream of the rotor tip trailing edge, and at 4.8, 21.4, and 32.2 percent chord axially downstream of the tip of the rotor blade trailing edge. The precision error in mean velocity LDV measurements ranged from 0.1 to 2.4 percent depending on the turbulence level. The measurement of radial velocity is not available.

### NUMERICAL APPROXIMATION

In this report, the centerline of the hub is defined as the  $X$ -axis of the coordinate system, with the positive direction being from upstream to downstream. The  $Z$  axis is chosen to lie in the vertical plane and is positive pointing upwards. The  $Y$  axis is chosen such that it forms a right-handed system with the  $X$  and  $Z$  axes. The positive tangential velocity points in the direction opposite to the direction of the rotating rotor (HIREP had a right-headed rotor, the rotor turned in clockwise direction while looking from downstream to upstream). The positive radial velocity points away from the hub.

## MOTION RELATIVE TO A ROTATING REFERENCE FRAME

Relative to a rotating reference frame, Newton's equations of motion, on which the Navier-Stokes equations are derived, are not directly applicable. In analyses, it is more convenient to specify the boundary conditions in terms of the rotating frame and to modify the equations of motion to accommodate the transformation to a non-inertial frame. To an observer fixed with the rotating frame, the expression for acceleration is no longer an invariant. The additional terms resulting from the transformation of reference frames appear as body forces and can be accounted for by introducing centrifugal and Coriolis forces. This statement can be expressed mathematically as follows:

$$\left(\frac{D\mathbf{u}}{Dt}\right)_I = \left(\frac{D\mathbf{u}}{Dt}\right)_R + \boldsymbol{\Omega} \times (\boldsymbol{\Omega} \times \mathbf{r}) + 2\boldsymbol{\Omega} \times \mathbf{u}_R \quad ,$$

where  $\mathbf{u}$  is the velocity vector,  $\boldsymbol{\Omega}$  is the angular velocity vector, and  $\mathbf{r}$  is the position vector. The subscripts I and R refer to inertial and rotating frames of reference. The term  $\left(\frac{D\mathbf{u}}{Dt}\right)_I$  is the actual acceleration that a fluid particle is experiencing, and  $\left(\frac{D\mathbf{u}}{Dt}\right)_R$  is the acceleration relative to the rotating frame;  $\boldsymbol{\Omega} \times (\boldsymbol{\Omega} \times \mathbf{r})$ , and  $2\boldsymbol{\Omega} \times \mathbf{u}_R$  are the centrifugal and Coriolis forces, respectively. At present, the flow variables in the rotor blade row are computed at a rotational frame of reference.

The three-dimensional incompressible RANS equations based on primitive variables are formulated in a boundary-fitted curvilinear coordinate system. Using Chorin's artificial compressibility formulation,<sup>9</sup> the incompressible Navier-Stokes equation is written in conservation law form for three-dimensional flow with the reference frame rotating about the  $X$ -axis at a constant angular velocity as,

$$Q_t + (E^* - E_v^*)_x + (F^* - F_v^*)_y + (G^* - G_v^*)_z + H = 0 \quad . \quad (1)$$

In Eq. 1 the dependent variable vector  $Q$  is defined as  $Q = (p, u, v, w)^T$  and the inviscid flux vectors  $E^*$ ,  $F^*$ , and  $G^*$ ; the viscous shear flux vectors  $E_v^*$ ,  $F_v^*$ , and  $G_v^*$ ; and the body forces,  $H$ , are given by

$$\begin{aligned} E^* &= (\beta u, u^2 + p, uv, uw)^T \\ F^* &= (\beta v, uv, v^2 + p, vw)^T \\ G^* &= (\beta w, uw, vw, w^2 + p)^T \\ E_v^* &= Re^{-1}(0, \tau_{xx}, \tau_{xy}, \tau_{xz})^T \\ F_v^* &= Re^{-1}(0, \tau_{yx}, \tau_{yy}, \tau_{yz})^T \\ G_v^* &= Re^{-1}(0, \tau_{zx}, \tau_{zy}, \tau_{zz})^T \\ H &= (0, -\Omega_x^2 y + \Omega_x \Omega_z, -\Omega_x^2 z - \Omega_x \Omega_y, 0)^T \quad . \end{aligned}$$

The coordinates  $x, y, z$  are scaled with an appropriate characteristic length scale  $L$ . The Cartesian velocity components  $u, v, w$  are nondimensionalized with respect to the free stream velocity,  $V_\infty$ . The  $X$  component of angular velocity,  $\Omega_x$ , is normalized with  $V_\infty$  and  $L$ , while the normalized pressure is defined as  $p = (p - p_\infty)/\rho V_\infty^2$ . The kinematic viscosity,  $\nu$ , is assumed to be constant, and the Reynolds number is defined as  $Re = V_\infty L/\nu$ . The artificial compressibility parameter,  $\beta$ , monitors the error associated with the addition of the unsteady pressure term  $\partial p/\partial t$  in the continuity equation which is needed for coupling the mass and momentum equations in order to make the system hyperbolic.

Equation 1 can be transferred to a curvilinear, body-fitted coordinate system  $(\zeta, \xi, \eta)$  through a coordinate transformation of the form

$$\zeta = \zeta(x, y, z), \quad \xi = \xi(x, y, z), \quad \text{and} \quad \eta = \eta(x, y, z) \quad .$$

Thus, Eq. 1 becomes,

$$(Q/J)_t + (E - E_v)_\zeta + (F - F_v)_\xi + (G - G_v)_\eta + (H/J) = 0 \quad (2)$$

with

$$(E, F, G)^T = \{ [T] \ (E^*/J, F^*/J, G^*/J)^T \}$$

and

$$(E_v, F_v, G_v)^T = [T] \ (E_v^*/J, F_v^*/J, G_v^*/J)^T \quad ,$$

where

$$[T] = \begin{bmatrix} \zeta_x & \zeta_y & \zeta_z \\ \xi_x & \xi_y & \xi_z \\ \eta_x & \eta_y & \eta_z \end{bmatrix}$$

and the Jacobian of the coordinate transformation is given by

$$J^{-1} = \det \begin{bmatrix} x_\zeta & y_\zeta & z_\zeta \\ x_\xi & y_\xi & z_\xi \\ x_\eta & y_\eta & z_\eta \end{bmatrix} \quad .$$

The Cartesian derivatives of the shear fluxes are obtained by expanding them using chain rule expansions in the  $\zeta, \xi$ , and  $\eta$  directions.

The basic operations of converting the set of differential equations to a system of difference equations may be divided into temporal differencing and spatial differencing. The procedure is described in the following sections.

## TEMPORAL DIFFERENCING

Because only the steady-state solutions are of interest, a first-order accurate Euler-implicit time differencing scheme is used. The application of the scheme avoids an overly restrictive time-step size when highly refined grids are used to resolve viscous effects. In addition, a spatially variable time step is used to accelerate convergence.

Defining computational cells with their centroids at  $l = \theta/\Delta\theta$  ( $\theta$  is  $\zeta$ ,  $\xi$ , or  $\eta$ ) and their cell interfaces at  $l \pm 1/2$ , the backward Euler time differencing of the three-dimensional conservation form is

$$\begin{aligned} \frac{\Delta Q^n}{J\Delta t} = & -[\Delta_\zeta(E^{n+1} - E_v^{n+1}) + \Delta_\xi(F^{n+1} - F_v^{n+1}) \\ & + \Delta_\eta(G^{n+1} - G_v^{n+1})] - H/J \end{aligned} \quad (3)$$

where  $\Delta t$  is the time step,  $\Delta Q^n = Q^{n+1} - Q^n$ , and  $\Delta_l(E) = [(E)_{l+1/2} - (E)_{l-1/2}]/\Delta\zeta$ . Superscripts denote the time level at which the variables are evaluated.

Linearizing Eq. 3 about time level  $n$ , we obtain

$$\begin{aligned} \left[ \frac{I}{J\Delta t} + \left( \frac{\partial E^n}{\partial Q} - \frac{\partial E_v^n}{\partial Q} \right) \Delta_\zeta + \left( \frac{\partial F^n}{\partial Q} - \frac{\partial F_v^n}{\partial Q} \right) \Delta_\xi \right. \\ \left. + \left( \frac{\partial G^n}{\partial Q} - \frac{\partial G_v^n}{\partial Q} \right) \Delta_\eta \right] \Delta Q^n = RHS \end{aligned} \quad (4)$$

where

$$RHS = -[\Delta_\zeta(E^n - F_v^n) + \Delta_\xi(F^n - F_v^n) + \Delta_\eta(G^n - G_v^n)] - H/J$$

and where  $I$  is the identity matrix.

## SPATIAL DIFFERENCING

The three-dimensional differential operator in Eq. 4 is first split into three independent one-dimensional operators. The spatial differencing of the inviscid flux in each of these one-dimensional operators is then constructed by an upwind flux differencing scheme based on Roe's approximate Riemann solver approach.<sup>10</sup> In each computational cell the differential operator is linearized around an average state such that the flux difference between two adjacent cells satisfies certain conservative properties. As a result, the flux at an interface can be expressed in terms of the directions of the travelling waves. Harten's high-resolution total variation diminishing (TVD) technique<sup>7</sup> is then applied to enhance the accuracy of the solution to a higher order in the region where its variation is relatively smooth. The undesirable spurious numerical oscillations associated with higher order approximations are suppressed by a limiter suggested by Wang and Richards.<sup>11</sup> This limiter is a modified Yee's version,<sup>7</sup> and is more suitable for viscous solutions at high Reynolds number. This approach is illustrated in the following section.

Letting the flux Jacobians  $A$ ,  $B$ , and  $C$  be defined as follows:

$$A \equiv \frac{\partial E^n}{\partial Q}, \quad B \equiv \frac{\partial F^n}{\partial Q}, \quad C \equiv \frac{\partial G^n}{\partial Q},$$

discretize the inviscid and viscous fluxes according to the upwind differencing scheme and to the central differencing scheme, respectively, in  $\xi$ ,  $\eta$ , and  $\zeta$  coordinate directions independently and then assemble them together. Equation 4 becomes

$$\begin{aligned} [(I/J\Delta t) &- (A^- + X)_{i+\frac{1}{2}}\Delta_{i+\frac{1}{2}} + (A^+ + X)_{i-\frac{1}{2}}\Delta_{i-\frac{1}{2}} \\ &- (B^- + Y)_{j+\frac{1}{2}}\Delta_{j+\frac{1}{2}} + (B^+ + Y)_{j-\frac{1}{2}}\Delta_{j-\frac{1}{2}} \\ &- (C^- + Z)_{k+\frac{1}{2}}\Delta_{k+\frac{1}{2}} + (C^+ + Z)_{k-\frac{1}{2}}\Delta_{k-\frac{1}{2}}] \Delta Q^n \\ &= -RES(Q^n) \end{aligned} \quad (5)$$

where  $i, j$ , and  $k$  are spatial indices associated with the  $\xi$ ,  $\eta$ , and  $\zeta$  coordinate directions, and  $A^\pm, B^\pm$ , and  $C^\pm$  are flux matrices split from the flux Jacobians  $A, B$ , and  $C$  according to the signs of their eigenvalues. The residual  $RES(Q^n)$  is evaluated with a TVD technique; the discretization is accurate to the third order. Conventional second-order central differencing is applied to obtain the viscous flux matrices  $X, Y$ , and  $Z$ . Equation 5 is solved by an implicit hybrid algorithm, where a symmetric planar Gauss-Seidel relaxation is applied in the streamwise direction  $\zeta$  in combination with approximate factorization in the remaining two coordinate directions  $\xi$  and  $\eta$  to avoid the  $\Delta t^3$  spatial splitting error incurred in fully three-dimensional approximate factorization methods. This scheme is unconditionally stable for linear systems and can be vectorized completely. As a result of upwind-differencing, the coefficient matrix of the system becomes diagonally dominant. In addition, the necessity of adding and tuning a numerical dissipation term for stability reasons, as in some schemes with central differencing, is alleviated.

## TURBULENCE MODEL

The Baldwin-Lomax algebraic turbulence model (BLM) is modified to simulate the turbulent effect of the flow. The BLM is applied to the blade-to-blade ( $\xi$ ) and spanwise ( $\eta$ ) directions independently. The mixing length  $l$  for the inner layer is calculated based on the distances from the end-wall ( $s_\eta$ ) and from the blade surface ( $s_\xi$ ):

$$l = \frac{2s_\xi s_\eta}{s_\xi + s_\eta + \sqrt{s_\xi^2 + s_\eta^2}}.$$

As suggested by Chima et al.<sup>12</sup> and Dorney and Davis,<sup>13</sup> the outer and the inner turbulence viscosities are combined by using Granville's blending function,<sup>14</sup> that is, the combined viscosity  $\mu$  is set to

$$\mu_o \tanh \frac{\mu_i}{\mu_o}$$

where  $\mu_o$  and  $\mu_i$  are the outer and inner viscosities, respectively. The turbulence velocity in the corner flow region is computed based on a blending function by Vatsa and Wedan<sup>15</sup>:

$$\mu = \frac{s_\eta^2 \mu_\xi + s_\xi^2 \mu_\eta}{s_\eta^2 + s_\xi^2}$$

In addition, the location of the wake center line is searched before the application of the BLM.

## GRID TOPOLOGIES AND BOUNDARY CONDITIONS

Grid topologies used to compute the IGV and rotor passage flow are similar. Essentially, the system includes three main blocks. There is a block of O-type grid around the blade; it is then connected upstream and downstream to two blocks of H-type grid that are extended to upstream boundary and downstream boundary planes, respectively. Through the overlapping cells at the connecting region, the solutions between the blocks communicate. In case of rotor passage, an additional block of H-type grid is used to cover the tip gap. For the O-type grid, there are 227 nodes around the blade surface, 33 nodes in the direction normal to the blade surface and 95 nodes from hub to casing. The upstream H-type grid contains 21 nodes in the axial direction, 39 nodes in the circumferential direction, and 95 nodes in the radial direction. The size of the downstream H-type grid is  $21 \times 77 \times 95$  in the axial, circumferential, and radial directions, respectively. The total number of the nodes for each blade passage is about 943,000.

The fillets at the blade hub/casing junctures are included in the gridding process. The grid spacings near the solid surface are selected such that the first  $y^+$  coordinate off the surface is about 1 or less. Figure 2 shows the surface grids in blade passages with every other grid in each coordinate direction removed. The periodicity conditions are applied along the bounding surfaces in the circumferential direction. At the upstream boundary plane, the velocity components are specified and the static pressure is extrapolated from the interior. At the downstream boundary plane, the static pressure is defined and the velocity components are extrapolated from the interior. On the solid surfaces, all components of velocity and the normal gradient of static pressure vanish. In addition, in the rotor passage, the tangential velocity on the surface of the nonrotating portion of the hub is prescribed according to the rotating speed of the rotor.

## SOLUTION PROCEDURE

In order to conserve the computational effort, the plenum region of the water tunnel is not modeled, only the region where the hub and casing are cylindrical is covered. The domain extends approximately from 1.5 IGV chord lengths upstream of the IGV

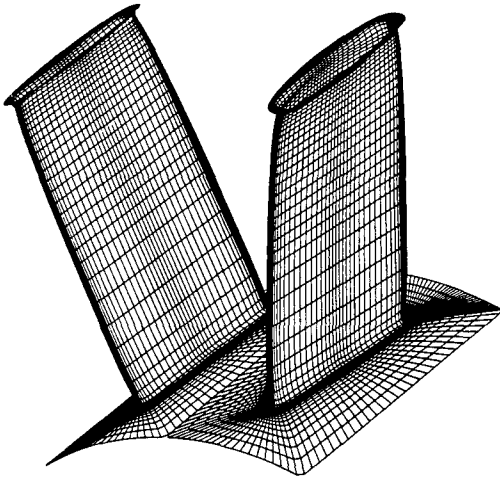


**Fig. 2a.** IGV passage.

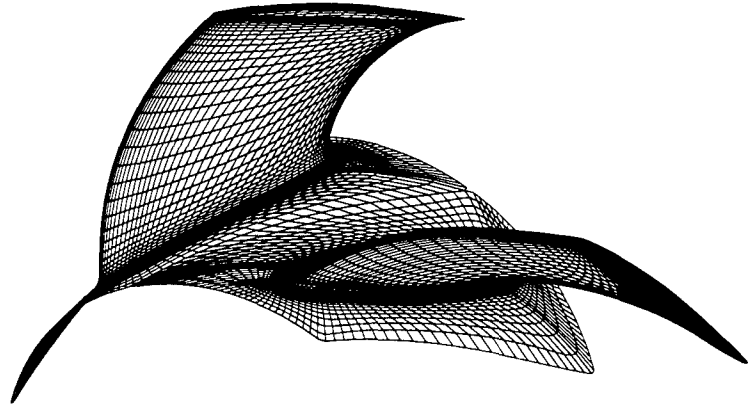


**Fig. 2.** Rotor passage.

**Fig. 2.** Surface grids in blade passages.

leading edge to approximately 2.5 IGV chord lengths downstream of the rotor blade trailing edge. All the measurements fall within this domain. Because only steady state solutions are of interest, a simplified iterative procedure is proposed. The procedure is described as follows:

1. Establish a computational domain including the IGV blade-to-blade passage. The grid system extended from 1.5 IGV chord lengths upstream of the blade leading edge to about 2.5 IGV chord lengths downstream of the IGV trailing edge. The inlet velocity distribution is assumed to be axisymmetrical and is similar to the  $1/7^{th}$  power boundary layer profile. It is then scaled such that the mass flow rate agrees with the measurement taken at 37 percent IGV chord upstream of the blade leading edge. The rotor effect can be approximated by distributing the body forces to the computational cells located within the rotor swept volume. The magnitude of the body forces is determined analytically based on the rotor characteristics. Use the grid system and the boundary conditions described earlier to obtain a converged solution.

A plane at 49.7 percent chord behind the trailing edge is defined as the stator exit plane. Circumferentially averaged solutions at that plane are then used as input for the rotor inlet plane.

2. Establish a computational domain including the rotor blade-to-blade passage. The grid system extends from 0.75 IGV chord lengths upstream of the blade leading edge to 2.5 IGV chord lengths downstream of the trailing edge. The axisymmetrical velocity profiles at the inlet plane are defined from the circumferentially averaged solution obtained at the exit plane in step 1. The solutions in the passage are then obtained by solving the equations of motion in the rotating reference frame.

Use the newly obtained circumferentially averaged static pressure at the inlet plane from step 2 as the pressure boundary condition at the exit plane for step 1 and repeat

the process. At present, the effort of performing a second iteration is minimum, because the interaction between the blade rows is small.

Computations were performed on a CONVEX 3080 mini supercomputer. For 930,000 nodes, each iteration required 2 minutes single processor CPU time. For each blade passage, it required 500 iterations to reach converged solutions ( $L_2$  norm of the residual drops by about three order of magnitude). To obtain above results, 700 iterations were carried out.

## RESULTS

The comparisons between the numerical results and the measurements are presented in the following sections.

### IGV PASSAGE

Due to the interaction of boundary layers from blades and wall surfaces (such as the hub and casing), the secondary flow is generated as the flow passes through the blade row passage. Secondary flow often appears in the form of vortices; common ones are horseshoe vortex, trailing edge vortex, passage vortex, corner vortex, and tip gap vortex. In this report, the secondary flow at a given plane is defined in the same manner as described by Zierke et al.<sup>1</sup> The local area-weighted circumferential mean at each spanwise location was computed and then was subtracted from the cross flow components at the same spanwise location. Figure 3a shows that some of the vortices mentioned previously can be identified clearly from the measurements taken at the HIREP experiment at 49.7 percent chord downstream of the trailing edge of the IGV. The computational result at the same location is shown in Fig. 3b. As the flow passes a blade section, the streamlines on the suction side of the blade tend to flow inward toward the location where the maximum lift occurs, while the streamlines on the pressure side of the blade tend to flow outward from the same location. As a result, a surface of discontinuity represented by a vortex sheet is formed as the flow leaves the trailing edge of the blade.

The IGV blade is designed such that the maximum lift occurs at 42 percent span. From the formation of the trailing edge vortex, Fig. 3b indicates that the computation predicts this location quite well. However, physically, the trailing vortex sheet is unstable. At a perturbation the sheet will roll up into a pair of vortex tubes rotating in opposite directions. Measurements shown in Fig. 3a suggest that such a process is taking place.

In the core region of the blade passage, a pressure gradient towards the suction surface is established to balance the circumferential acceleration. As a first order approximation, it can be assumed that the same pressure gradient exists throughout the boundary layers near the hub and casing surfaces. For a given pressure gradient, the smaller the velocity, the smaller the radius that the particle will follow; this is the case

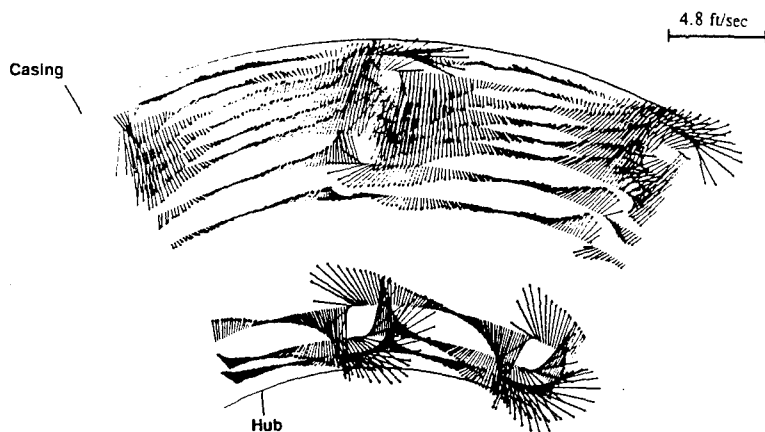


Fig. 3a. Measurements with five-hole probe.

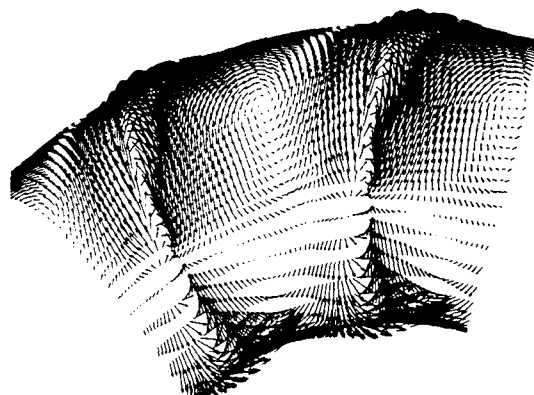
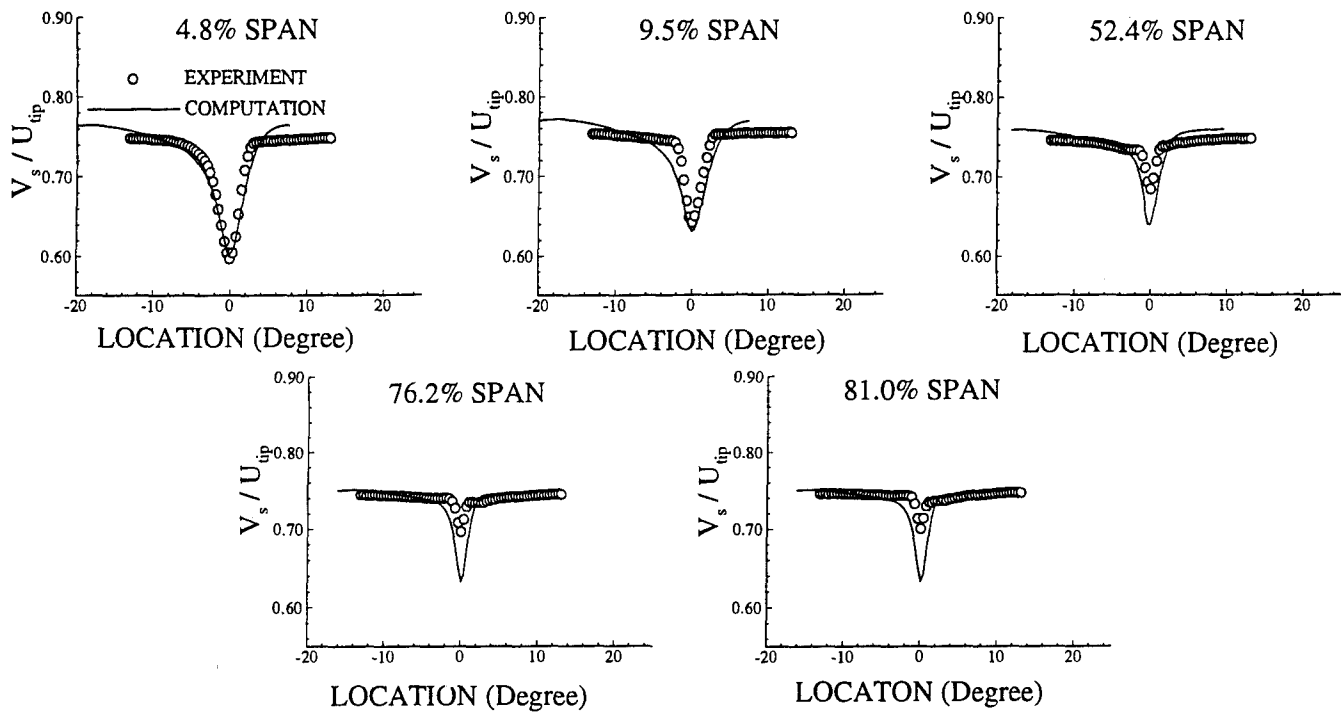


Fig. 3b. Computation.

Fig. 3. Secondary velocity vectors 49.7 percent chord axially downstream of the IGV trailing edge.

in the wall boundary layers. Therefore, near the walls, the slower moving flow is forced toward the suction side from the pressure side. This mechanism generates two passage vortices of opposite sign between the blades that can be found in Fig. 3a and Fig. 3b. As discussed in Zierke et al.,<sup>1</sup> the trailing vortex sheets and the passage vortices coexist. One is not actually the cause of the other. For the present case, the strengths of the passage vortices are weak, as can be indicated by the flow visualizations on the hub and casing surfaces. Boundary layers at hub/casing surfaces separate in front of the leading edge of the blades, and horseshoe vortices are generated. The pressure side lag of the horseshoe vortex has the same sign as the passage vortex and will merge into the passage vortex. Figures 2 and 3 present no evidence of the horseshoe vortices at 49.7 percent chord downstream from the trailing edge. Perhaps, their strengths are greatly reduced through the interaction with other vortices.

Figure 4 shows the comparison of the measured and computed IGV wakes at several spanwise locations. The measuring plane is 49.7 percent chord axially downstream of the IGV trailing edge. The streamwise velocity  $V_s$  is defined as the vector sum of the velocities in the axial ( $V_x$ ) and tangential directions ( $V_t$ ). The experimental data presented are passage-averaged. Error bars are computed and reported in Zierke et al.<sup>1</sup> Near the hub at 4.8 percent span and 9.5 percent span the wakes are wider, deeper, and asymmetric due to the boundary layer interaction at the blade/hub region. Computations display the same characteristics, and the agreement with the measurements is very good. Farther away from the hub surface, the wakes become shallower and more symmetric. Computations show the same trend but with somewhat deeper deficits. Figure 5 shows the circumferentially-averaged velocity components at 49.7 percent chord axially downstream of the IGV trailing edge. Two sets of measurement are shown in the figure, one was obtained with radial probe and the other with wake rake. Uncertainty analysis by Zierke et al.<sup>1</sup> shows that the wake rake data are more reliable.



**Fig 4.** Passage-averaged IGV wakes 49.7 percent chord axially downstream of the IGV trailing edge.

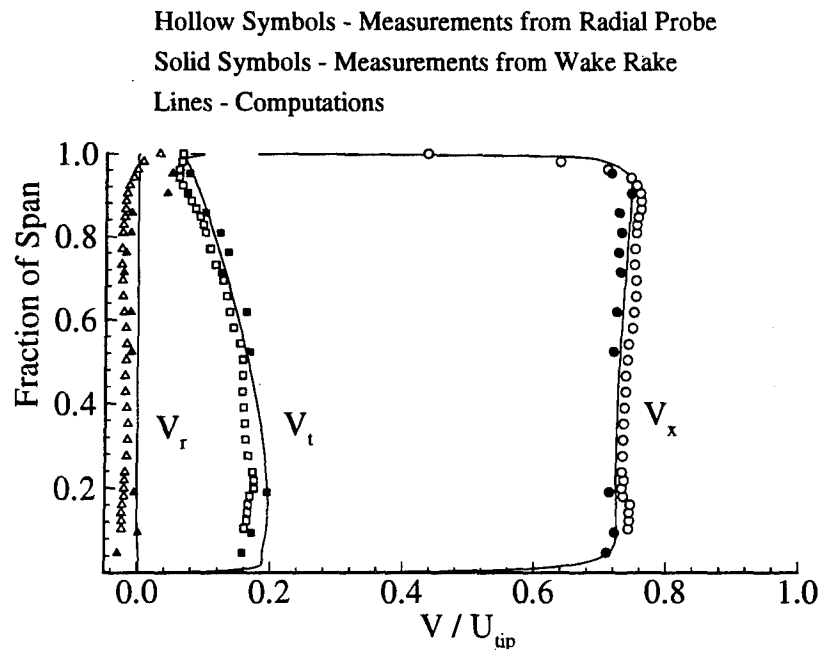


**Fig. 5.** Circumferentially averaged velocities 49.7 percent chord axially downstream of the IGV trailing edge.

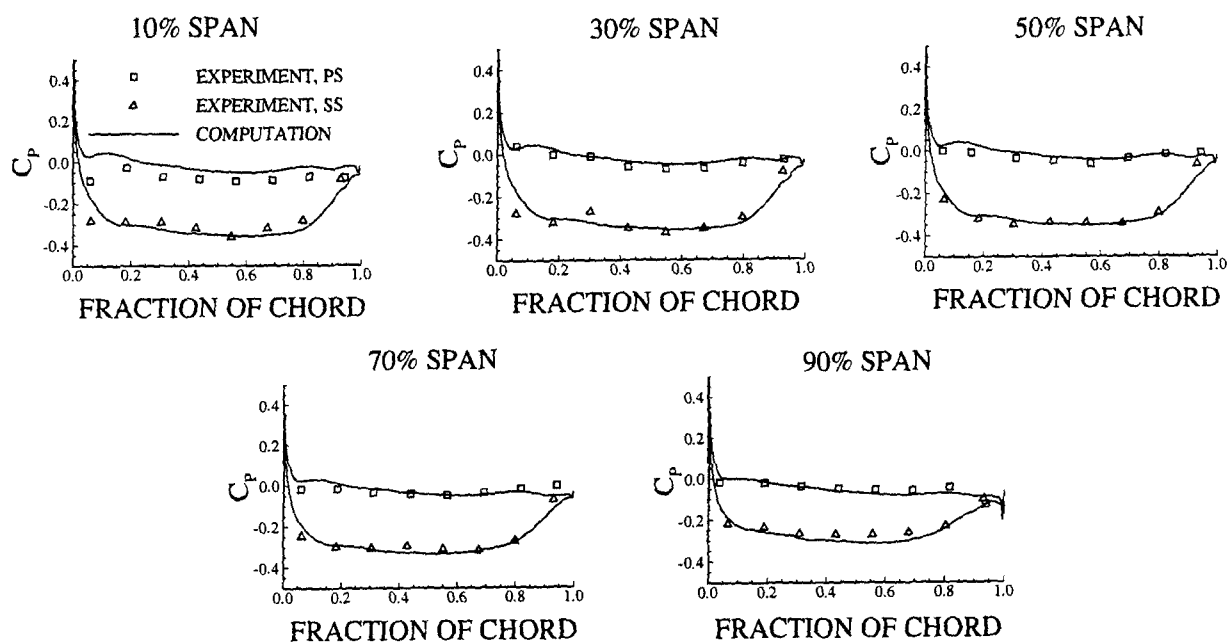
Figure 6 shows the static pressure distribution on the IGV blade surface. The pressure coefficient is normalized by a dynamic pressure based on blade tip speed as defined by Zierke et al.<sup>1</sup> At 10 percent span, near the leading edge, the measured pressures at both suction and pressure side are lower than those computed. The same discrepancy was found in the lifting surface calculation<sup>1</sup> and in Dreyer and Zierke's viscous flow computation.<sup>2</sup> Computations agree well with measurements at other spanwise locations.

Figure 7 shows the flow visualization on the hub surface. The locations of the saddle points at the hub surface near the leading and trailing edges are predicted correctly. Figure 8a shows the flow visualization on the blade pressure side surface. Both computation and experiment show no flow separation on the surface. Figure 8b shows the flow visualization on the blade suction side surface. Experiments indicate that flow separates upstream of the trailing edge with corner vortices. The predicted separation line is slightly downstream of the observed line except near the casing where the predicted separation is further upstream than that observed.

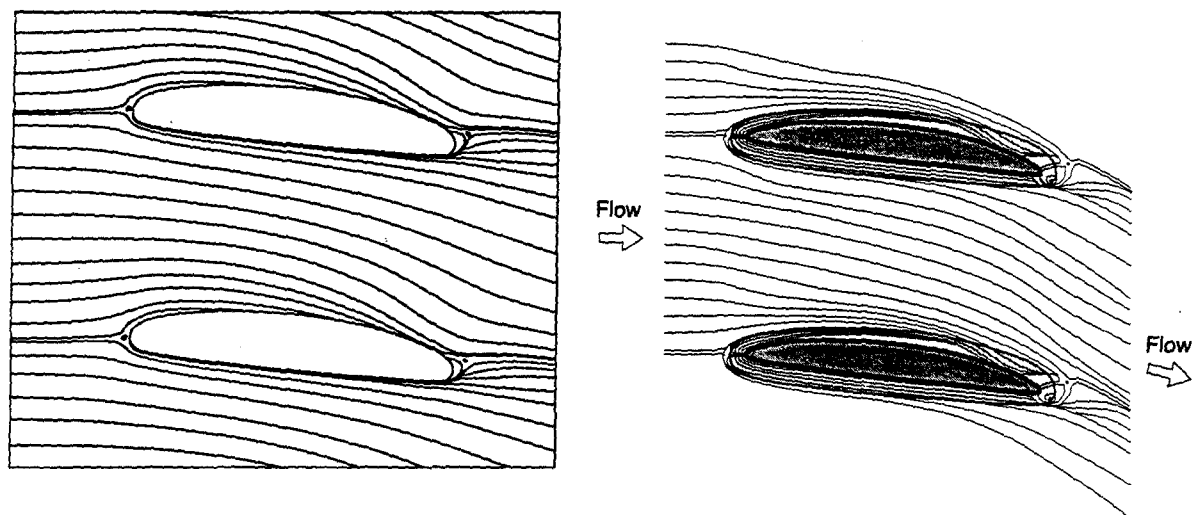
## ROTOR PASSAGE

Figure 9 shows the comparison of the measured and computed rotor wakes in different spanwise locations. The measuring plane is 32.3 percent chord axially downstream of the rotor tip trailing edge. At each spanwise location, the axial ( $V_x$ ) and tangential ( $V_t$ ) velocity components are measured with the LDV method around 360 deg at 0.5 deg intervals. The spatial repeatability of the measurements among all seven blade passages is excellent; only two cycles of representative data are shown in Fig. 9. The agreement between the measurement and the computation is very good from 20 percent span to near 80 percent span. Note that the maximum lift on the blade is designed to occur at about 22 percent of span. At locations closer to the hub surface, computed wakes have larger than measured deficits. At locations near the casing end-wall, the velocity peak at mid-pitch is not predicted very well.

Figure 10 shows the static pressure distribution on the rotor surface. Figure 11 shows the computed secondary velocity vectors (Fig. 11a) and streamlines (Fig. 11b) at a plane 37.8 percent chord axially downstream of the rotor tip trailing edge (looking from downstream to upstream). The blade wake can be identified by the locations where the vectors have large negative (in the direction of blade rotation) tangential components. Due to the relative motion between the blade and the end-wall, the blade scrapes up the end-wall boundary layer in front of it as it advances. As a result, a scraping vortex is formed.<sup>16</sup> In Fig. 11, the trace of the scraping vortex can be located ahead of the blade wake. Trailing behind the blade wake near the end-wall is the tip leakage vortex. The passage vortices between the blades and the horseshoe vortex system at the blade/hub juncture can also be identified. Figure 12 shows the flow visualization on hub surface. The location of the saddle point ahead of the leading edge is predicted correctly. The predicted location of the saddle point near the trailing edge is further downstream than observed. Figure 13 shows the flow visualization on the blade suction surface.



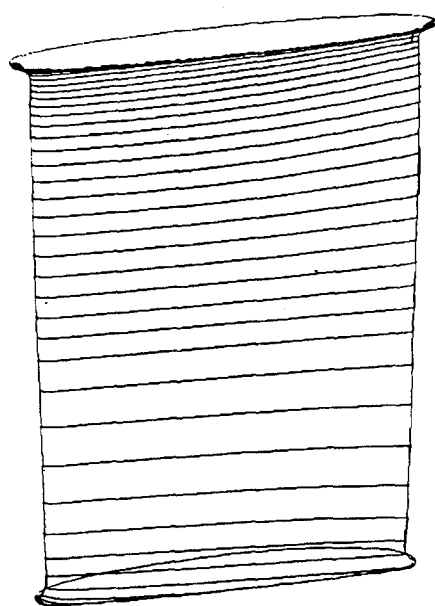
**Fig. 6.** Static pressure distribution on the IGV blade surface.



**Fig. 7a.** Computation.

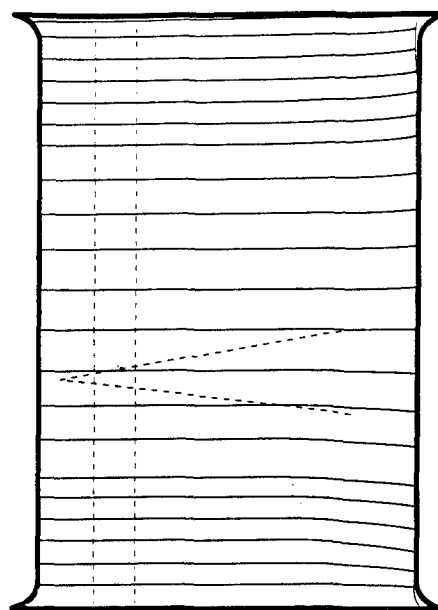
**Fig. 7b.** Experiment.

**Fig. 7.** Surface flow visualization on the IGV hub surface.



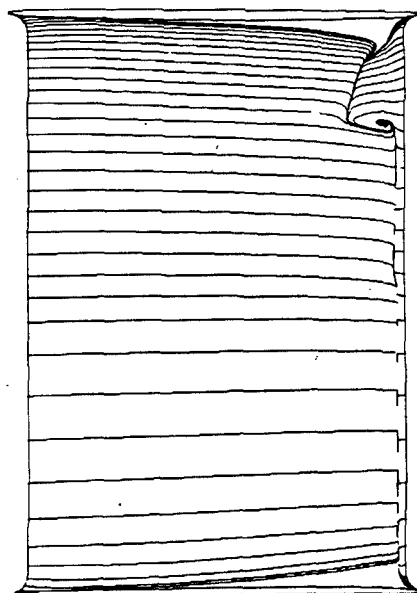
**COMPUTATION**

Flow  
→



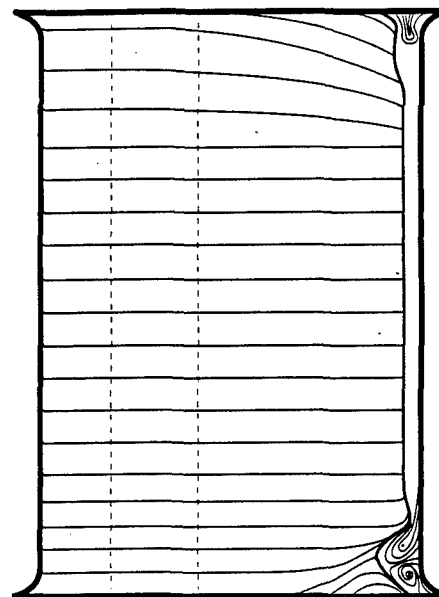
**EXPERIMENT**

**Fig. 8a. Pressure side surface.**



**COMPUTATION**

Flow  
→



**EXPERIMENT**

**Fig. 8b. Suction side surface.**

**Fig. 8. Surface flow visualization on the IGV blade surface.**

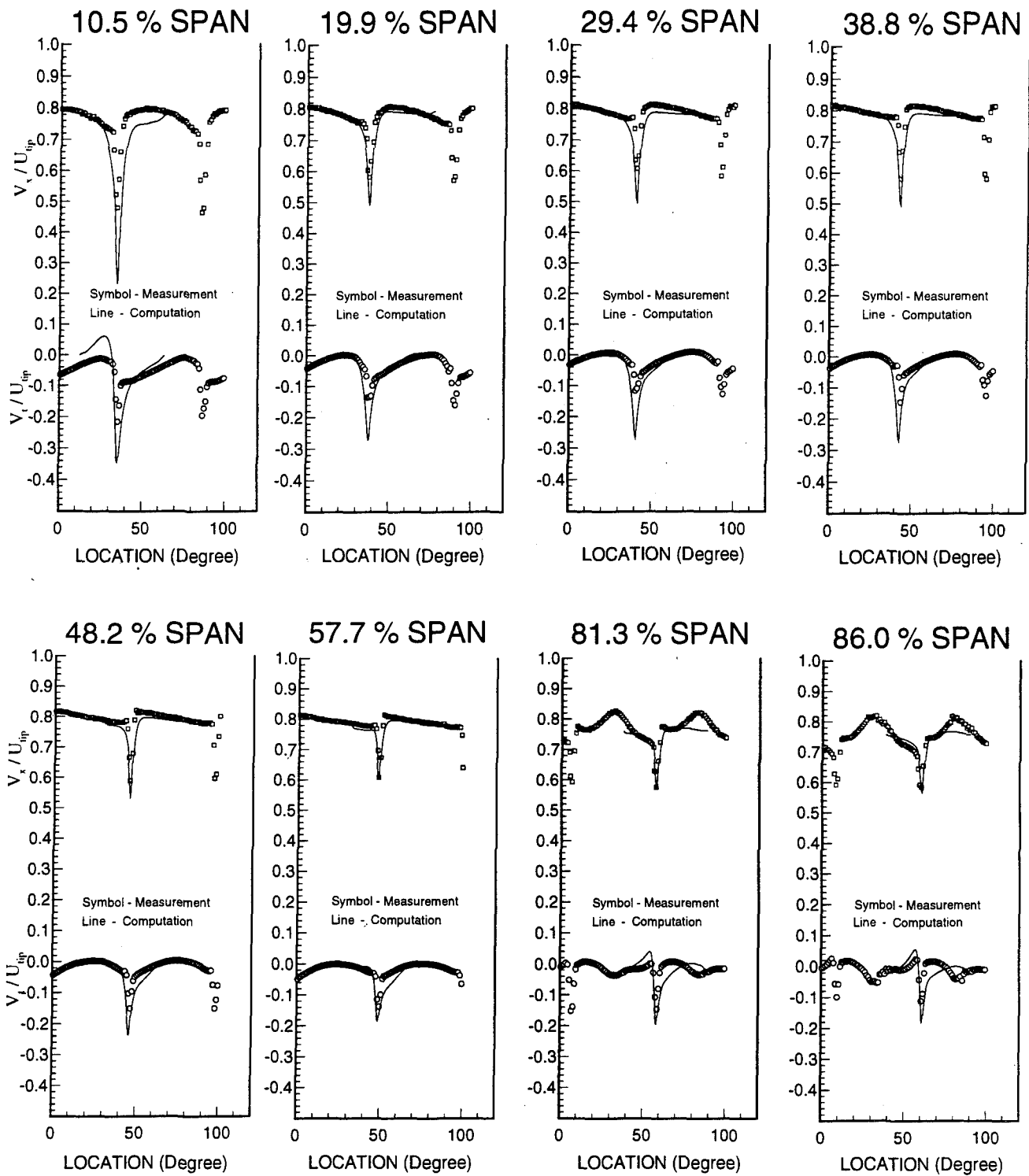


**Fig. 9.** Circumferential variation of velocity components 32.2 percent chord axially downstream of the rotor tip trailing edge.

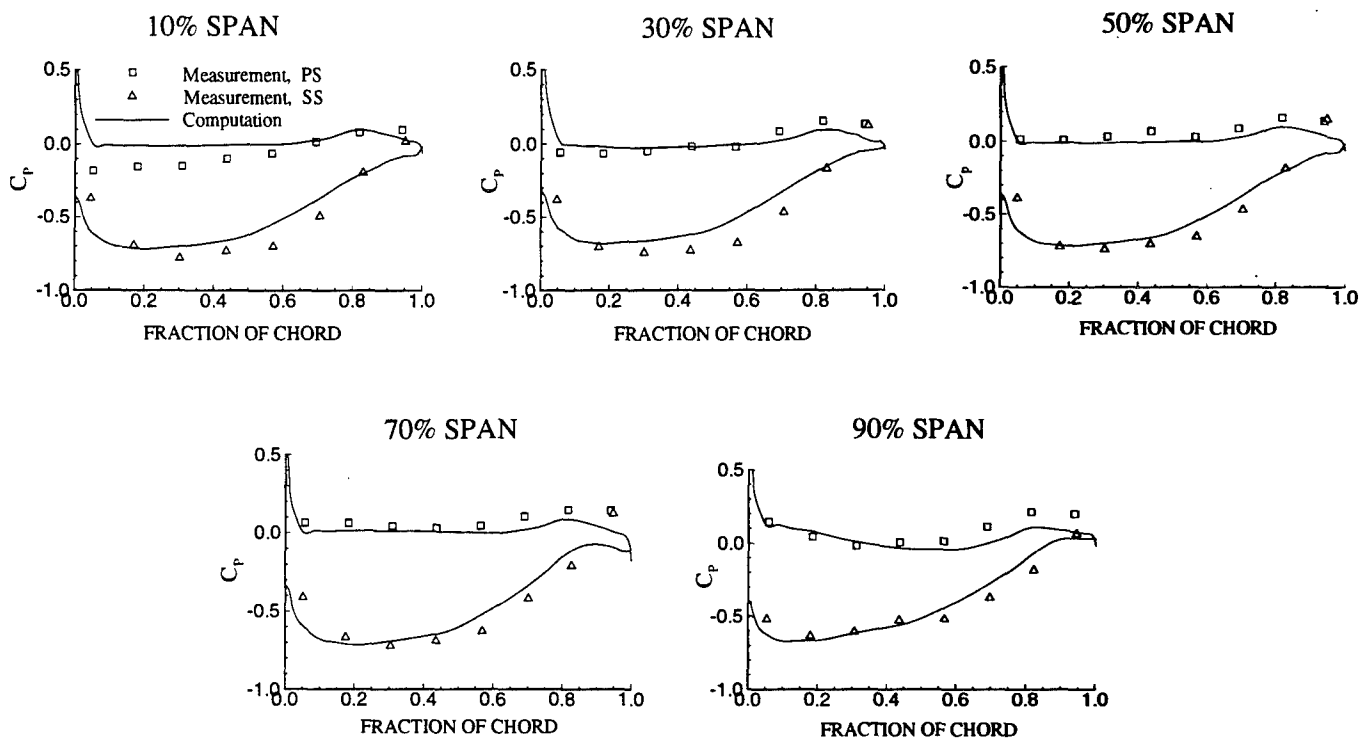


Fig. 10. Static pressure distribution on the rotor surface.

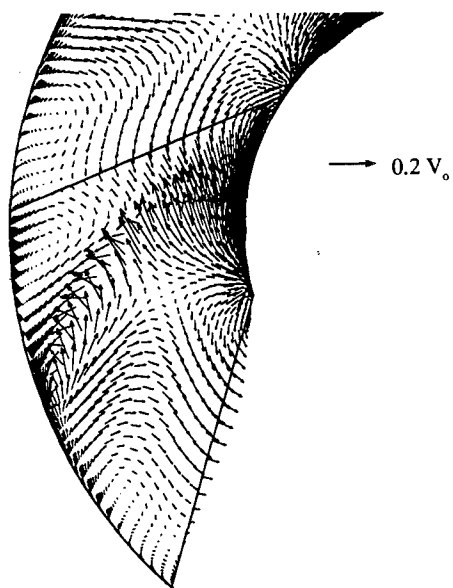


Fig. 11a. Computed vectors.

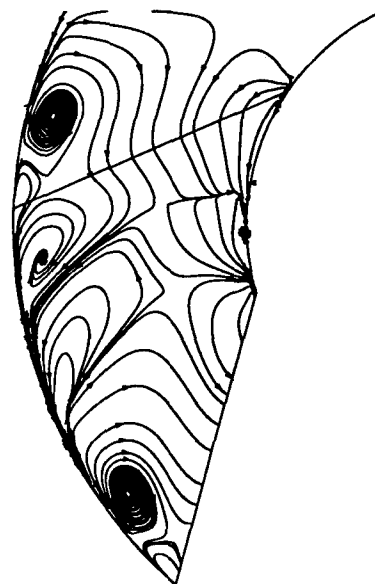
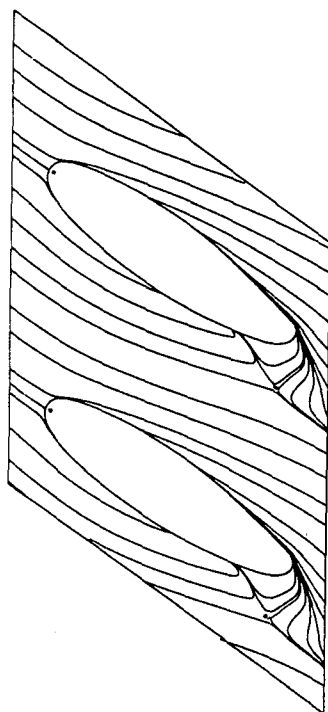
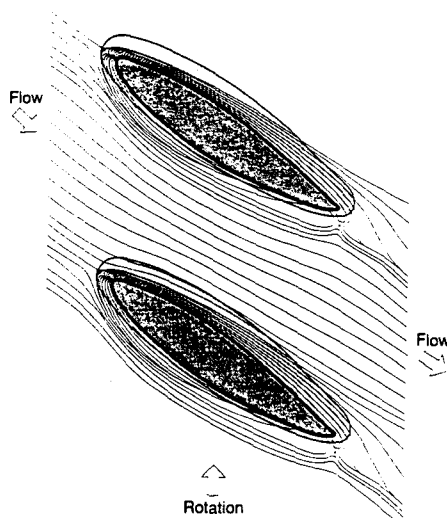


Fig. 11b. Particle traces.

Fig. 11. Predicted secondary velocity at 37.8 percent chord axially downstream of the rotor tip trailing edge.



**Fig. 12a. Computation.**



**Fig. 12b. Experiment.**

**Fig. 12. Surface flow visualization on the rotor hub surface.**

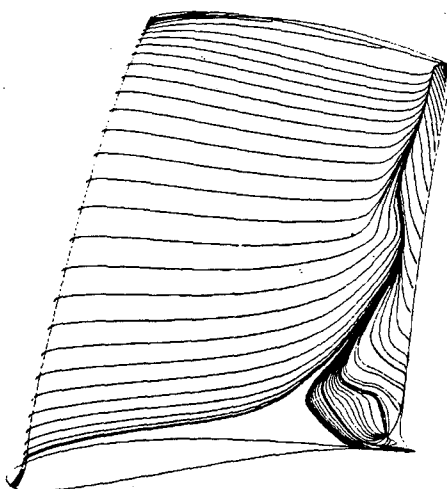


**Fig. 13a. Computation.**

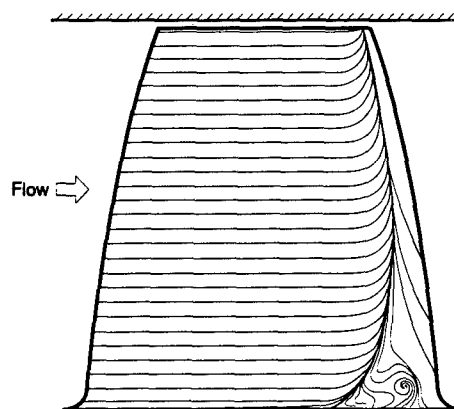


**Fig. 13b. Experiment.**

**Fig. 13. Surface flow visualization on the suction side surface of the rotor blade.**

It indicates that trailing edge separation vortex moves radially up the trailing edge. The predicted separation line agrees well with the observed line. Figure 14 shows the particle traces of flow through the tip gap from the pressure side to the suction side of the blade. Vorticity is formed and shedded along the suction surface. A similar phenomenon was observed in an experiment by Farell<sup>17</sup> and predicted by Dreyer and Zierke.<sup>2</sup>

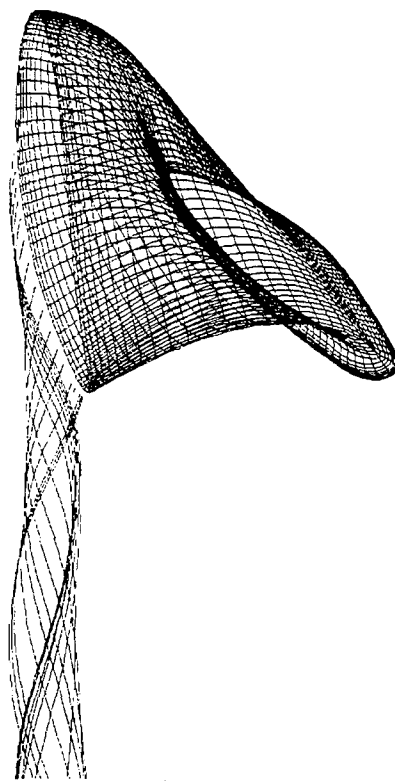


**Fig. 14.** Particle traces of the flow through rotor tip gap.

## CONCLUSIONS AND RECOMMENDATIONS

An implicit high-resolution finite-differencing scheme to obtain a steady-state solution for flow passing a multiple-blade-row turbomachinery is shown. In the scheme flows through stator and rotor passages were solved separately, and then were coupled through iteration processes.

The surface flow visualizations indicate that the flow separations on the hub and blade surfaces are predicted correctly, although the details of the surface imprint of the corner vortices near the junctures are not captured. The visualizations further suggest that the flow near the end-wall surfaces turns from the pressure side of the blades toward the suction side of the blades. However, the turning motion, that can

be associated with the formation of a passage vortex, is relatively mild in comparison with those occurring in the turbine passages. Because of the relative weakness of the passage vortex, the predicted secondary flow pattern behind the IGV agrees well with the inviscid solution presented by Zierke et al.<sup>1</sup> In the rotor passage, because of the relative motion between the rotor blade and the casing, the tip gap vortex behind the blade and the scraping vortex in front of the blade are predicted.

## CONCLUSIONS

Comparisons between the computed and the measured static pressures on the IGV and the rotor blade surfaces show that the loading distributions are predicted reasonably well. The wakes behind the IGV are predicted reasonably well even near the hub juncture. Overall, the predicted wake deficits are somewhat deeper than those measured. The predicted and measured rotor wakes disagree near the hub and casing, but better agreements exists at mid-span region.

## RECOMMENDATIONS

The computations for rotor passage were carried out in a rotating reference frame. In order to improve the prediction, the effects of rotation to the turbulence modeling require some special considerations. Some useful suggestions can be found in a report by Gorski.<sup>18</sup>

## REFERENCES

1. Zierke, W. C., Strake, W. A., and Taylor, P. D., "The High Reynolds Number Flow Through a Axial-Flow Pump," Technical Report TR 93-12, ARL/PSU (1993).
2. Harten, A., "High Resolution Scheme for Hyperbolic Conservation Laws," *Journal of Computational Physics*, Vol. 49, No. 3, pp. 357-393 (1983).
3. Yee, H., "Implicit Total Variation Diminishing (TVD) Scheme for Steady-State Calculation," *Journal of Computational Physics*, Vol. 57, pp. 327-360 (1985).
4. Hartwich, P-M, and Hsu, C-H, "High-Resolution Upwind Scheme for the Three-Dimensional Incompressible Navier-Stokes Equations," *AIAA Journal*, Vol. 26, No. 11 (Nov 1988).
5. Dreyer, D. J., and Zierke, W. C., "Solution of the Average-Passage Equations for the Incompressible Flow through Multiple-Blade-Row Turbomachinery," Technical Report TR 94-05, ARL/PSU (1994).
6. Lee, Y-T, Hah, C., and Loellbach, J., "Flow Analyses in a Single-Stage Propulsion Pump," ASME Paper 94-GT-139 (1994).

7. Adamczyk, J. J., Celestina, M. L., Beach, T. A., and Barnett, M., "Simulation of 3-D Viscous Flow within a Multi-Stage Turbine," ASME Paper 89-GT-152 (1989).
8. Hah, C., "Calculation of Three-Dimensional Viscous Flows in Turbomachinery with a Implicit Relaxation Method," *Journal of Propulsion and Power*, Vol. 3, No. 5, pp. 415-422 (1987).
9. Chorin, A., "A Numerical Method for Solving Incompressible Viscous Flow Problem," *Journal of Computational Physics*, Vol. 2, pp. 2-26 (1967).
10. Roe, P. L., "Approximate Riemann Solvers, Parameter Vectors, and Difference Scheme," *Journal of Computational Physics*, Vol. 43, No.2, PP. 357-372 (1981).
11. Wang, Z., Richards, B. E., "High Resolution Scheme for Steady Flow Computation," *Journal of Computational Physics*, Vol. 97, pp. 53-72 (1991).
12. Chima, R. V., Giel, P. W., and Boyle, R. J., "An Algebraic Turbulence Model for Three-Dimensional Viscous Flows," Technical Report AIAA 93-0083, 31st Aerospace Sciences Meeting Exhibit (Jan 1993).
13. Dorney, J. J., and Davis, R. L., "Navier-Stokes Analysis of Turbine Blade Heat Transfer and Performance," *Journal of Turbomachinery*, Vol. 114, pp. 795-806 (Oct 1992).
14. Granville, P. S., "A Near-Wall Eddy Viscosity Formula for Turbulent Boundary Layers in Pressure Gradients Suitable for Momentum, Heat or Mass Transfer," ASME *Journal of Fluids Engineering*, Vol. 112, pp. 25-28 (1990).
15. Vasta, V. N., and Wedan, B. W., "Navier-Stokes Solutions for Transonic Flow Over a Wing Mounted in a Wind Tunnel," Technical Report 88-0102, AIAA (1988).
16. Phillips, W. R. C., and Head, M. C., "Flow Visualization in the Tip region of a Rotating Blade Row," *Int. J. Mech. Sci.*, Vol. 22, pp. 495-521 (1980).
17. Farrell, K. J., "An Investigation of End-Wall Vortex Cavitation in High Reynolds Number Axial-Flow Pump," M.S. Thesis, Department of Mechanical Engineering, Pennsylvania State University (May 1989).
18. Gorski, J. J., "Application of the David Taylor Navier-Stokes (DTNS) Code in Non-Inertial reference Frames," CDNSWC-SHD-1362-01, Carderock Division, Naval Surface Warfare Center, Bethesda, MD (Sep 1992).



# INITIAL DISTRIBUTION

Copies	Code	Name	Copies	Code	Name
1	ARPA	G. Jones	4	PSU/ARL	
			1	C. Knight	
6	ONR		1	McBride	
1	333	J. Fein	1	D. Thompson	
1	333	P. Majumdar	1	W. Zierke	
1	333	P. Purtell			
1	333	E. Rood			
1	334	A. Tucker			
1	334	R. Vogelsong			

## CENTER DISTRIBUTION

Copies	Code	Name	Copies	Code	Name
1	OPNAV		1	0114	K. Kim
1	N87S	J. Schuster			
8	NAVSEA		1	50	W.B. Morgan
1	03H	E. Comstock	1	508	R. Boswell
2	03X	R. Crockett	1	508	J. Brown
1	03T	M. Nicholson	1	508	R. Cross
1	PEO-SUB R	A. Spero	1	508	H. Liu
1	PEO-SUB R	M. Troffer	1	521	W. Day
1	PEO-SUB R	E. Robinson	1	542	J. Gorski
1	PEO-SUB X	L. Becker	1	542	C-H Sung
1	PEO-SUB X	D. Goldstein	1	542	H. Haussling
			1	542	Y.-T. Lee
2	NUWS		1	544	F. Peterson
1	P. Lefebvre		1	544	C. Dai
1	J. Uhlman		1	544	B. Chen
			1	544	S. Neely
2	DTIC		1	544	D. Fuhs
			1	544	C-I Yang
1	Science Applications International Corp.		1	7051	W. Blake
1	R. Korpus		1	7200	Y-F Hwang
3	MIT/Dept. Ocean Eng.		1	3421	TIC (C)
1	D. Keenan				
1	J. Kerwin				
1	S. Kinnas				
1	Newport News Shipbuilding				
1	J. DeNuto				
1	General Dynamics/EB Div.				
1	M. King				
1	Arete Associates				
1	T. Brockett				